Long-Term Vicarious Calibration of GOSAT Short-Wave Sensors: Techniques for Error Reduction and New Estimates of Radiometric Degradation Factors

Akihiko Kuze, Thomas E. Taylor, Fumie Kataoka, Carol J. Bruegge, David Crisp, Masatomo Harada, Mark Helmlinger, Makoto Inoue, Shuji Kawakami, Nobuhiro Kikuchi, Yasushi Mitomi, Jumpei Murooka, Masataka Naitoh, Denis M. O'Brien, Christopher W. O'Dell, Hirofumi Ohyama, Harold Pollock, Florian M. Schwandner, Kei Shiomi, Hiroshi Suto, Toru Takeda, Tomoaki Tanaka, Tomoyuki Urabe, Tatsuya Yokota, and Yukio Yoshida

***Abstract*—This work describes the radiometric calibration of the short-wave infrared (SWIR) bands of two instruments aboard the Greenhouse gases Observing SATellite (GOSAT), the Thermal And Near infrared Sensor for carbon Observations Fourier Transform Spectrometer (TANSO-FTS) and the Cloud and Aerosol Imager (TANSO-CAI). Four vicarious calibration campaigns (VCCs) have been performed annually since June 2009 at Railroad Valley, NV, USA, to estimate changes in the radiometric response of both sensors. While the 2009 campaign (VCC^{2009}) indicated significant initial degradation in the sensors compared to the prelaunch values, the results presented here show that the stability of the sensors has improved with time. The largest changes were seen in the 0.76 μm oxygen A-band for TANSO-FTS and in the 0.380 and 0.674 μm bands for TANSO-CAI. This paper describes techniques used to optimize the vicarious calibration of the GOSAT SWIR sensors. We discuss error reductions, relative to previous work, achieved by using higher quality and more comprehensive *in situ* measurements and proper selection of reference remote sensing products from the Moderate Resolution Imaging Spectroradiometer used in radiative transfer calculations to model top-of-the-atmosphere radiances. In addition, we present new estimates of TANSO-FTS radiometric degradation factors derived by combining the new vicarious calibration results with the time-dependent model provided by Yoshida *et al.* (2012), which is based on analysis of on-board solar diffuser data. We conclude that this combined model provides a robust correction for TANSO-FTS Level 1B spectra. A detailed error budget for TANSO-FTS vicarious calibration is also provided.**

***Index Terms*—Carbon dioxide (CO_2), Greenhouse gases Observing SATellite (GOSAT), short-wave infrared (SWIR), Thermal And Near infrared Sensor for carbon Observations (TANSO), vicarious calibration.**

I. Introduction

THE Greenhouse gases Observing SATellite (GOSAT), launched on January 23, 2009, carries two independent sensors, the Thermal And Near infrared Sensor for carbon Observations Fourier Transform Spectrometer (TANSO-FTS) and the Cloud and Aerosol Imager (TANSO-CAI) [1], [2]. Carbon dioxide (CO_2) and methane (CH_4) are retrieved from the TANSO-FTS spectra collected in the 0.765 μm oxygen (O_2) A-band (B1), the weak CO_2 and CH_4 bands between 1.60 and 1.68 μm (B2), and the strong CO_2 band near 2.06 μm (B3). Simultaneously, TANSO-CAI provides an image of the scene with measurements in the ultraviolet at 0.38 μm (B1), in the visible red at 0.674 μm (B2), in the near infrared at 0.870 μm (B3), and in the short-wave infrared (SWIR) at 1.60 μm (B4). The relatively high spatial resolution of TANSO-CAI (0.5 km for B1–B3 and 1.5 km for B4) allows for robust cloud screening of the TANSO-FTS spectra [3]. Note that TANSO-FTS is also equipped with a thermal infrared band, the calibration of which was discussed in [4].

Accurate radiometric calibration of the GOSAT solar band sensors is needed to distinguish the reflection from the Earth's surface and scattering by aerosols and thin clouds. If a time-dependent degradation is neglected, the surface reflectance retrieved from the satellite data is underestimated, and the optical path length uncertainties from scattering by thin clouds

Manuscript received February 12, 2013; revised July 20, 2013; accepted August 6, 2013.

A. Kuze, M. Harada, S. Kawakami, J. Murooka, M. Naitoh, K. Shiomi, H. Suto, T. Takeda, and T. Urabe are with the Japan Aerospace Exploration Agency, Tsukuba 305-8505, Japan (e-mail: kuze.akihiko@jaxa.jp).

T. E. Taylor was with the Cooperative Institute for Research in the Atmosphere, Colorado State University, Fort Collins, CO 80523-1375 USA. He is now with the Department of Atmospheric Science, Colorado State University, Fort Collins, CO 80523-1375 USA.

F. Kataoka and Y. Mitomi are with the Remote Sensing Technology Center of Japan, Tsukuba 305-0032, Japan.

C. J. Bruegge, D. Crisp, M. Helmlinger, H. Pollock, and F. M. Schwandner are with the Jet Propulsion Laboratory, California Institute of Technology, Pasadena, CA 91109-8099 USA.

M. Inoue, N. Kikuchi, T. Yokota, and Y. Yoshida are with the National Institute for Environmental Studies, Tsukuba 305-8506, Japan.

D. M. O'Brien was with the Cooperative Institute for Research in the Atmosphere, Colorado State University, Fort Collins, CO 80523-1375 USA. He is now with O'Brien R&D LLC, Livermore, CO 80536 USA.

C. W. O'Dell is with the Department of Atmospheric Science, Colorado State University, Fort Collins, CO 80523-1375 USA.

H. Ohyama was with the Japan Aerospace Exploration Agency, Tsukuba 305-8505, Japan. He is now with the Solar-Terrestrial Environment Laboratory, Nagoya University, Nagoya 464-8601, Japan.

T. Tanaka was with the Japan Aerospace Exploration Agency, Tsukuba 305-8505, Japan. He is now with the Ames Research Center, National Aeronautics and Space Administration, Moffett Field, CA 94035 USA.

Color versions of one or more of the figures in this paper are available online at http://ieeexplore.ieee.org.

Digital Object Identifier 10.1109/TGRS.2013.2278696

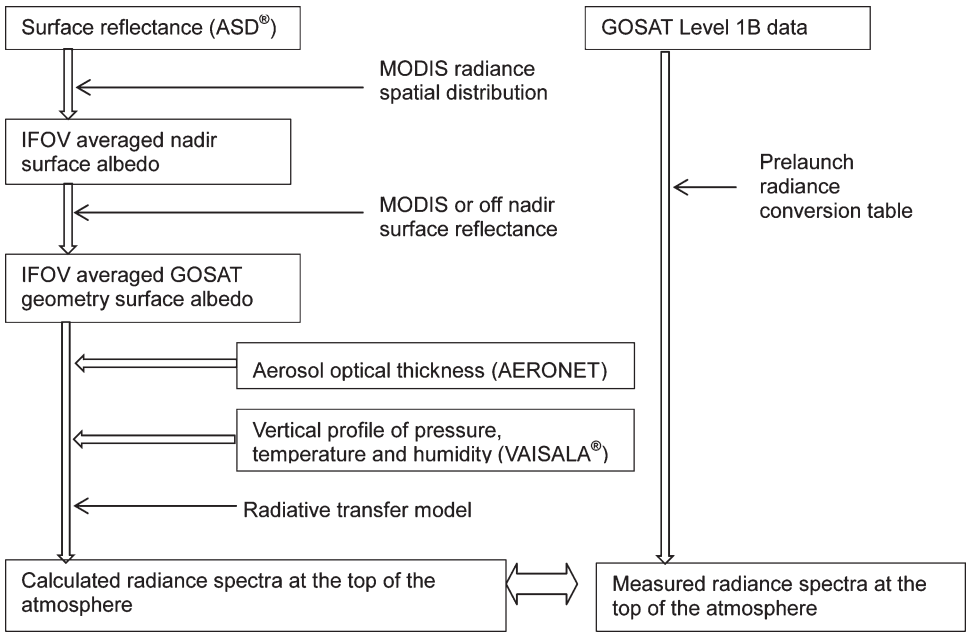

Fig. 1. Flow diagram for the vicarious calibration of GOSAT.

and aerosols become relatively large. This introduces both systematic and random errors in the retrieved surface pressure and column CO_2 and CH_4 values [5]–[7].

The GOSAT sensors are subject to radiometric degradation as associated with contamination of the optics and losses in optical efficiency that may occur in the FTS mechanism of TANSO-FTS [2]. Vicarious calibration campaigns (VCCs) have been undertaken annually at the Railroad Valley (RRV) desert playa, NV, USA (38.497° N, 115.691° W, 1437 m above mean sea level), to monitor the radiometric calibration of the GOSAT sensors. *In situ* measurements collected during the campaigns at RRV are used in radiative transfer codes to simulate radiance spectra at the top of the atmosphere (TOA). The modeled spectra are then compared with nearly simultaneous measurements taken by the TANSO-FTS and TANSO-CAI on GOSAT. A summary of VCC^{2009}, including the selection of sites, the meteorological measurements, and the calculation of the radiometric degradation factors (RDFs), was first described in [8]. The early results indicated degradations in TANSO-FTS of about 11%, 2%, and 3% in B1, B2, and B3, respectively, when averaging the P and S polarizations. The combined root-mean-square (rms) error was determined to be approximately 7% in all bands and polarizations. For TANSO-CAI, the change in instrument response was estimated at -17%, $+4\%$, 0%, and -18% for B1–B4, respectively, with rms errors of 6% in all bands.

Here, we provide updated estimates of the RDFs for both TANSO-FTS and TANSO-CAI using the combined measurements and knowledge from four VCCs. In Section II, we give a brief overview of the vicarious calibration method and techniques for minimizing the error. In Section III, the radiometric degradation of the TANSO-FTS sensor is discussed, while Section IV covers the degradation analysis of TANSO-CAI. A detailed error budget is presented in Section V. Finally, discussion and conclusions are given in Section VI.

II. Vicarious Calibration Method and Error Reduction

Since the launch of GOSAT in January 2009, four VCCs have been performed as a joint effort by the Japan Aerospace Exploration Agency (JAXA) GOSAT team and the National Aeronautics and Space Administration-sponsored Atmospheric Carbon Observations from Space (ACOS) team. In this section, we briefly describe the method and discuss techniques used to improve both the accuracy and precision of the calibration. A flow diagram of the analysis is shown in Fig. 1. In short, GOSAT Level 1B (L1B) spectra are converted into radiance units by application of prelaunch calibration factors, which are tied to absolute standards [1], [9]. These measured radiance spectra are then regressed against a set of TOA modeled radiance spectra, calculated via a radiative transfer code using measured ground, radiosonde, and the Moderate Resolution Imaging Spectroradiometer (MODIS) data as inputs.

Table I lists each day of VCC^{2009} through VCC^{2012} and gives a brief summary of the atmospheric conditions over the playa. TANSO-FTS views RRV in target mode from GOSAT orbit paths 36 (over UT) and 37 (over CA). The viewing times are 20:44 and 21:16 UTC with slant angles of 19.9° and 33.0°, respectively. Unlike TANSO-FTS, TANSO-CAI has a wide swath of $\pm 36.1°$ for bands 1–3 with 500-m spatial resolution and has a 1500-m spatial resolution over a $\pm 30.0°$ swath for band 4. Therefore, from path 36, all four bands lie within the field of view (FOV) of TANSO-FTS, whereas from path 37, only bands 1–3 cover RRV. Nine 500 m $\times$ 500 m ground sites were selected via an analysis of the spatial uniformity of the TANSO-CAI band 3 measured reflectance. Each day during a field campaign, the surface reflectance was measured using Analytical Spectral Devices (ASD) spectrometers at two distinct ground sites near the time of GOSAT overpass. Meteorological data (pressure, temperature, and humidity) from a surface weather station and a radiosonde launch, and aerosol optical thicknesses (AOTs)

TABLE I
LIST OF THE DAYSIDE GOSAT OVERPASSES DURING THE VCCs AND SELECTION OF DATA SETS

Year	Date	Path	Radiosonde	Weather and comments	Site	Retain Former criteria	New criteria
2009	06-23	36	Yes	Clear	H03	N	N
				Bad L1b spectra	L06	Y	N
	06-24	37	Yes	Clear	H03	Y	N
					L06	Y	N
	06-26	36	No	Cloudy	H03	N	N
					M03	N	N
	06-27	37	Yes	Clear	H03	Y	N
					L08	Y	N
	06-29	36	No	Cloudy	H03	N	N
					H14	N	N
	07-02	36	Yes	Heavy AM rain	H03	Y	N
				Clear in PM	H14	Y	Y
	07-03	37	Yes	Overnight rain	H03	N	N
					L04	Y	Y
	07-05	36	Yes	Clear	H03	Y	Y
					M20	Y	Y
2010	06-21	36	Yes	Clear	M03	–	N
					L08	–	Y
	06-22	37	Yes	Clear	M03	–	N
					L04	–	N
	06-24	36	No	Partial cloud cover	M03	–	N
					H14	–	N
	06-25	37	No	Complete cloud cover	M03	–	N
2011	06-19	36	Yes	AM rain	M03	–	N
				Partial cloud in PM	L08	–	N
	06-20	37	Yes	Clear	M03	–	N
					L08	–	N
	06-22	36	Yes	Small cloud fraction	M03	–	N
					L04	–	N
	06-23	37	Yes	Clear	M03	–	N
					H14	–	Y
	06-25	36	Yes	Clear	M03	–	N
					M20	–	N
	06-26	37	Yes	Clear	M03	–	N
					H21	–	Y
2012	06-25	36	No	Clear	M03	–	N
	06-26	37	No	Clear	M03	–	N
					L08	–	N
	06-28	36	Yes	Clear	M03	–	Y
					H14	–	Y
	06-29	37	Yes	Clear	M03	–	Y
					M20	–	Y
	07-01	36	Yes	Clear	M03	–	Y
					L04	–	Y
	07-02	37	Yes	Clear	M03	–	Y
					MODIS	–	Y

measured at the AErosol RObotic NETwork (AERONET) site stationed at RRV [10], were collected for use in the radiative transfer codes needed to model TOA radiances.

A. Summary of VCCs and Improvements

The general VCC methods for the large instantaneous FOV (IFOV) of the GOSAT TANSO-FTS ($\simeq$10.5-km diameter at nadir) and TANSO-CAI (500 m $\times$ 500 m) were detailed in [8]. For VCC^{2009}, the ASD spectrometer, used to derive the surface reflectance, was carried by an operator with the foreoptics mounted on a rod extending $\simeq$1 m horizontally, as depicted in Fig. 2(a) and (b). This setup made it difficult to collect consistent and reliable measurements due to operator fatigue and unpredictable behavior. Beginning with VCC^{2010}, the ASD spectrometer and computer were mounted on a rolling cart, as depicted in Fig. 2(c), to reduce the error in the measurements.

Further error reduction in the derived reflectances was achieved by performing more frequent calibration against the Spectralon reference panels to reduce the time interval for interpolation. For VCC^{2010} and VCC^{2011}, the Spectralon panels were placed directly on the ground rather than using a tripod mount. The longer distance between the ASD input sensor and the ground ($\simeq$0.7 m) increased the sensitivity to

(a) VCC^{2009}.

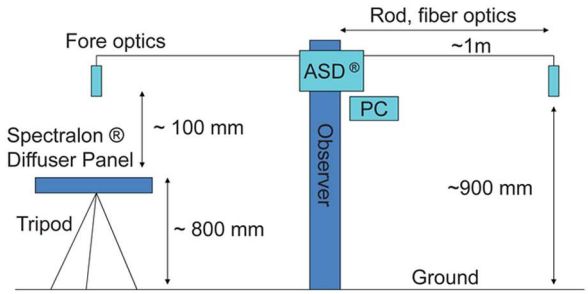

(b) VCC^{2009}.

(c) VCC^{2010}-VCC^{2011}.

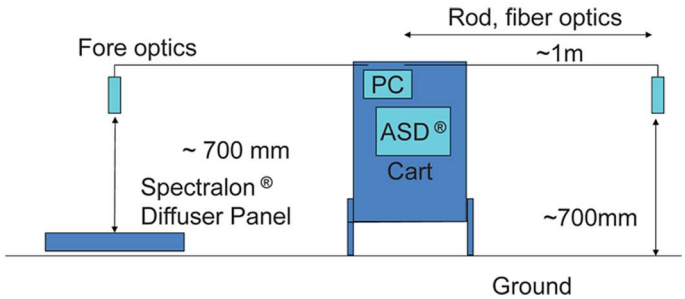

(d) VCC^{2010}-VCC^{2011}.

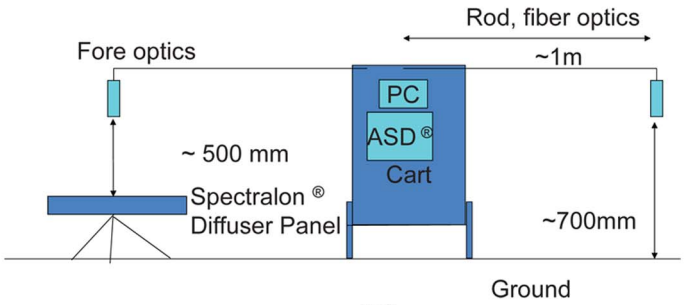

(e) VCC^{2012}

Fig. 2. Configuration for the ASD spectrometer measurements used in the vicarious calibration of the GOSAT sensors. (a) Photograph of the original configuration used for VCC^{2009}. (b) Configuration used for VCC^{2009} when the operator carried the ASD controlling computer and sensor in a harness with the foreoptics mounted on a horizontal pole. (c) Photograph of the configuration used during VCC^{2010} through VCC^{2012}, with the ASD controlling computer and sensor mounted in a cart. (d) Configuration used for VCC^{2010} and VCC^{2011} using the cart but with the Spectralon panel set directly on the ground. (e) Configuration used for VCC^{2012} with the Spectralon panel set on a small tripod.

the alignment between the ASD FOV and the Spectralon target. We hypothesize that the ASD sometimes viewed desert surface during Spectralon reference measurements. This would explain why many data sets failed a statistical threshold analysis in 2010 and 2011; see Section II-B for more details. For VCC^{2012}, the Spectralon panels were mounted on a tripod so that the distance between the ASD foreoptics and panel was $\simeq$0.5 m, and careful alignment was performed. This resulted in the best data set of the four years.

Other techniques were adopted over the course of the four field campaigns to reduce the uncertainty in the calibration.

1) The ASD warm-up time prior to beginning measurements was increased to 2 h to improve stability.
2) The grid was optimized such that the measurement sequence could be completed in $\simeq$60 min rather than 120 min needed during VCC^{2009}. These minimized solar zenith angle (SZA) and bidirectional reflectance distribution function (BRDF) change during the measurement sequence.
3) ASD measurements at grid box corners were suspended to avoid ground disturbed by foot traffic, which often has lower reflectance.
4) More frequent dark count subtractions were made during the measurement time periods.
5) Fine tuning of the TANSO-FTS pointing angles using the on-board camera image was conducted before the campaign to more accurately target the RRV playa.

TABLE II
VALUES USED IN THE ASD STATISTICAL THRESHOLD TESTS. THE MEAN (μ) AND STANDARD DEVIATION (σ) ARE USED TO CALCULATE THE COEFFICIENT OF VARIATION (η)

Threshold description	Variable	Threshold value B1	B2	B3
Coefficient of variation in scaled Spectralon® spectra	$\eta_V^S = \sigma^S/\mu^S$	< 0.01	< 0.01	< 0.02
Coefficient of variation in the calculated reflectance time series	$\eta_V^R = \sigma^R/\mu^R$	< 0.05	< 0.035	< 0.04
Slope of linear least squares (LLS) fit to calculated reflectance time series	$\lvert m \rvert$	< 0.02	< 0.02	< 0.035

6) Simultaneous observations were made with uplooking wide-FOV pyranometers to detect subvisible cirrus clouds.

B. ASD Reflectance Measurements

Surface reflectances needed for the radiative transfer modeling were derived from the ASD measurements using essentially the same methods described in [8, Sec. II-D]. Some improvements have been made to the technique since the first campaign in 2009. For example, as noted earlier, some ASD data were discarded due to issues such as incorrect leveling and alignment of the Spectralon reference panel or high scatter in the measurements. For each annual data set, a set of rigorous statistical threshold tests was performed to determine which ASD sites should be retained for the vicarious calibration analysis. Three sets of criteria were established based on the VCC^{2012} data set, as summarized in Table II. The thresholds presented here correspond to the 99% confidence interval, i.e., $\mu + 2.58\sigma$ with mean μ and standard deviation σ. The rightmost column in Table I indicates pass or fail of each ASD data set in the record based on this statistical threshold testing.

C. Use of MODIS Radiance and BRDF Products

As discussed in [8, App.], the MODIS half-kilometer radiance product (MYD02HKM) is used to scale the small ASD grid box up to the larger TANSO-FTS footprint. Selection of a particular MODIS granule was done by analyzing the MODIS cloud product to find a scene for each year that meets the following new criteria:

1) cloud free (no visible cirrus flags, cirrus reflectance $< 1.5\%$, and cloud fraction $= 0$);
2) sensor viewing $< 20^\circ$ (to minimize the MODIS pixel size and best match the ASD geometry);
3) MODIS granule time within ± 35 min of both GOSAT overpass 36 and 37 times.

Table III lists the MODIS radiance granule selected for each year and the relevant cloud and reflectance values. The four MODIS pixels nearest to the ASD grid box were weighted by the inverse of the distance from the center, to determine a more representative reflectance value than provided by a single MODIS pixel (as was done in the original VCC^{2009} analysis). The RDFs at individual data points were shifted by up to 0.015 (1.5% change in radiometric correction), with 0.005 being a typical change. The random scatter due to the new method yielded minimal change in the mean RDFs. However, a small decrease in the range of the RDF scatter was observed, particularly for VCC^{2009} and VCC^{2012}.

The surface reflectance derived from the ASD measurements requires a correction using the BRDF, since GOSAT views the playa from a nonnadir angle, while the ASD measurements are made at nadir. See [8, App.] for a detailed description of how the correction is implemented during the scaling of the ASD grid box to the full size of the TANSO-FTS footprint. In this study, the MODIS 16-day MCD43B1 BRDF product is used [11], [12]. This kernel-driven model linearly combines an isotropic parameter with a volume scattering component and a surface scattering/geometric shadow casting component. For each year, a single distinct granule was selected for use in the VCC analysis, as shown in Table IV. Some of these 16-day products likely contain 1 or more days with a wet surface at the RRV test site, based on the rain gauge data taken at the

TABLE III
SELECTION OF MODIS HALF-KILOMETER RADIANCE GRANULES USED TO SCALE ASD SURFACE REFLECTANCE TO THE TANSO-FTS FOOTPRINT. ΔT GIVES THE TIME DIFFERENCE IN MINUTES, $\mathcal{F}_{ci}$ REPRESENTS THE VISIBLE CIRRUS FLAG, F_{ci} REPRESENTS THE CIRRUS FRACTION, AND F_{cl} REPRESENTS THE CLOUD FRACTION. THE MEAN MODIS REFLECTANCE AT SELECT BANDS AND THE COEFFICIENT OF VARIATION ARE GIVEN BY $\overline{\mathcal{R}}_B$ AND $\overline{\eta}_B$, RESPECTIVELY

MODIS granule	ΔT	θ_{sat}	$\mathcal{F}_{ci}$	F_{ci}	F_{cl}	$\overline{\mathcal{R}}_B$	$\overline{\eta}_B$
2009174.2050						$\overline{\mathcal{R}}_{B1}$=0.383	$\overline{\eta}_{B1}$=0.127
(June 23, 2009)	+5/-25	7.6°	N	0.004	0.000	$\overline{\mathcal{R}}_{B2}$=0.402	$\overline{\eta}_{B2}$=0.127
						$\overline{\mathcal{R}}_{B3}$=0.350	$\overline{\eta}_{B3}$=0.162
2010177.2045						$\overline{\mathcal{R}}_{B1}$=0.403	$\overline{\eta}_{B1}$=0.058
(June 26, 2010)	0/+30	7.0°	N	0.003	0.000	$\overline{\mathcal{R}}_{B2}$=0.434	$\overline{\eta}_{B2}$=0.047
						$\overline{\mathcal{R}}_{B3}$=0.378	$\overline{\eta}_{B3}$=0.067
2011173.2040						$\overline{\mathcal{R}}_{B1}$=0.359	$\overline{\eta}_{B1}$=0.062
(June 22, 2011)	-5/-35	19.2°	N	0.004	0.000	$\overline{\mathcal{R}}_{B2}$=0.385	$\overline{\eta}_{B2}$=0.059
						$\overline{\mathcal{R}}_{B3}$=0.331	$\overline{\eta}_{B3}$=0.075
2012183.2045						$\overline{\mathcal{R}}_{B1}$=0.389	$\overline{\eta}_{B1}$=0.044
(July 1, 2012)	0/-30	7.0°	N	0.013	0.000	$\overline{\mathcal{R}}_{B2}$=0.417	$\overline{\eta}_{B2}$=0.038
						$\overline{\mathcal{R}}_{B3}$=0.371	$\overline{\eta}_{B3}$=0.058

Notes: Times are given relative to GOSAT overpass paths 36/37 times, i.e., positive (+) indicates MODIS after GOSAT, while minus (-) indicates MODIS before GOSAT.
Reflectances are given for MODIS bands 620-670 nm (B2), 1628-1652 nm (B6) and 2105-2155 nm (B7).

TABLE IV
SELECTION OF MODIS MCD43B1 BRDF GRANULE AND RAINFALL DATA (DUCKWATER, NV, USA) USED TO CORRECT THE ASD MEASUREMENTS FOR SURFACE BRDF EFFECTS

Year	MODIS granule	Start Date	End Date	Rain Event	Accumulated Rainfall
2009	2009185.h08v05	July 4	July 19	July 18	$\simeq$ 2 mm
2010	2010161.h08v05	June 10	June 25	June 11-13	$\simeq$ 2 mm
2011	2011169.h08v05	June 18	July 3	June 18-19	$\simeq$ 2 mm
2012	2012161.h08v05	June 9	June 24	None	0.0 mm

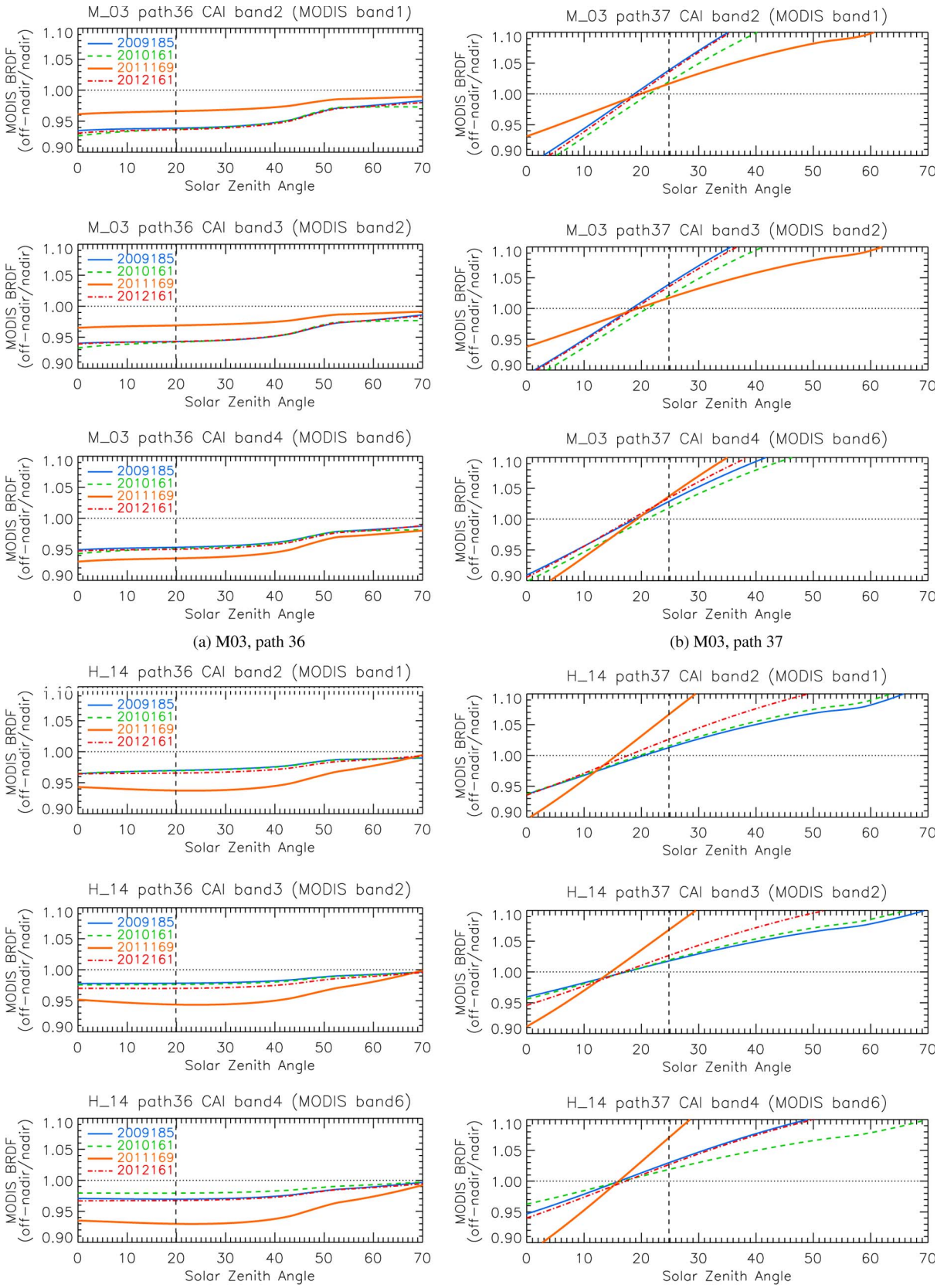

(a) M03, path 36

(b) M03, path 37

(c) H14, path 36

(d) H14, path 37

Fig. 3. Ratios of the MODIS off-nadir versus nadir BRDF values as a function of SZA on 2 days at two different ASD sites. The three plots in each panel correspond to TANSO-CAI spectral (top) band 2 (0.67 μm), (middle) band 3 (0.87 μm), and (bottom) band 4 (1.6 μm). (a) and (b) are both for site M03, which has a soft surface, viewed from GOSAT paths 36 and 37, respectively. (c) and (d) are both for site H14, which has a hard surface, viewed from GOSAT paths 36 and 37, respectively. The four colored lines represent the MODIS granules listed in Table III used in the VCC analysis. The vertical dashed lines indicate the SZA at the time of GOSAT overpass.

TABLE V
ESTIMATED RDFS FOR TANSO-FTS FROM THE RRV VCCS RELATIVE TO THE PRELAUNCH CALIBRATION

	B1				B2				B3			
	Short ν_1		Long ν_1		Short ν_2		Long ν_2		Short ν_3		Long ν_3	
Year	P	S	P	S	P	S	P	S	P	S	P	S
2009	0.871	0.855	0.865	0.845	0.956	0.941	0.948	0.933	0.951	0.935	0.951	0.933
2010	0.855	0.835	0.853	0.828	0.946	0.930	0.939	0.924	0.938	0.918	0.936	0.914
2011	0.852	0.846	0.852	0.842	0.954	0.947	0.946	0.940	0.930	0.919	0.932	0.919
2012	0.821	0.804	0.820	0.801	0.949	0.939	0.941	0.931	0.951	0.936	0.952	0.935
2010-2009	-0.016	-0.020	-0.012	-0.017	-0.010	-0.010	-0.009	-0.009	-0.013	-0.017	-0.015	-0.019
2011-2009	-0.019	-0.009	-0.013	-0.004	-0.002	0.007	-0.002	0.007	-0.021	-0.016	-0.019	-0.014
2012-2009	-0.050	-0.050	-0.045	-0.044	-0.007	-0.002	-0.007	-0.002	0.000	0.001	0.002	0.001

Notes: Short ν_1 corresponds to frequency range 12900-13050 cm^{-1}.
Long ν_1 corresponds to frequency range 13050-13200 cm^{-1}.
Short ν_2 corresponds to frequency range 6150-6225 cm^{-1}.
Long ν_2 corresponds to frequency range 6225-6300 cm^{-1}.
Short ν_3 corresponds to frequency range 4800-4850 cm^{-1}.
Long ν_3 corresponds to frequency range 4850-4900 cm^{-1}.

nearby Duckwater station, NV, USA, located approximately 65 km northwest of RRV.

The MODIS BRDF product at RRV shows a stronger SZA dependence for backscattered solar reflections, as observed from GOSAT path 37 [Fig. 3(b) and (d)] and as compared to forward-scattered solar reflections observed from path 36 overpasses [Fig. 3(a) and (c)]. The potential for errors related to the BRDF correction is therefore larger for GOSAT path 37 overpasses than for path 36 overpasses. Analysis of the MODIS BRDF model also indicates that harder surfaces [site H14 shown in Fig. 3(c) and (d)] are more diffuse, i.e., more Lambertian, than softer surfaces [site M03 shown in Fig. 3(a) and (b)]. Furthermore, the surface BRDF has been found to be sensitive to ground moisture (i.e., recent rainfall), which changes the spectral reflectance characteristics of the surface, particularly for harder surfaces as seen in the MCD43B1 2011169 data set (the orange lines in Fig. 3).

During VCC^{2010}, the ground-based Portable Apparatus for Rapid Acquisition of Bidirectional Observation of the Land and Atmosphere (PARABOLA) was used to measure BRDFs *in situ* [13]. PARABOLA is a 4π-scanning radiometer that is mounted on a 5-m vertical mast, taking measurements at eight channels in 5° azimuth and zenith increments. A direct comparison of the BRDF measured by PARABOLA at 1.65 μm to the MODIS product at 1.60 μm indicates differences of at worst 10%, with some dependence on zenith and azimuth viewing angles.

III. DEGRADATION ESTIMATE FOR TANSO-FTS SWIR BANDS

A. Estimation of Radiometric Degradation

The analysis described in this work uses the most recent version of the JAXA L1B data (V150.151), which has been continuously released since April 2012. The previous GOSAT calibration results that were published in [8] were reprocessed using the new version of the L1B files.

The technique for estimating the RDFs of the TANSO-FTS SWIR bands is essentially the same as that presented in [8, Sec. V]. We assume that the atmospheric and surface properties are sufficiently well characterized such that the differences between the measured radiance y_i and the modeled radiance x_i at any wavelength i can be approximated as $y_i = mx_i$, where m is the RDF. Assuming that m is constant over a range of wavelengths $i = 1, \ldots, N$, the RDFs are determined via a χ^2 minimization of the sum of the squared differences between the measured and modeled radiances

$$\chi^2 = \sum_{i=1}^{N} [y_i - mx_i]^2. \tag{1}$$

The RDF for a particular spectral region (λ) and polarization $(\mathrm{P}|\mathrm{S})$ is given by the least squares solution

$$\mathrm{RDF}_{\lambda,\mathrm{P|S}} = m_{\lambda,\mathrm{P|S}} = \frac{\sum_i [x_i \cdot y_i]}{\sum_i x_i^2}. \tag{2}$$

The explicit spectral and polarization dependence of x_i and y_i has been omitted on the right-hand side (RHS) of (2) to avoid clutter. In this work, the measured radiances were first corrected by the TANSO-FTS prelaunch calibration. Therefore, all RDFs are given relative to the instrument's sensitivity prior to launch, unless otherwise noted. Spectra are organized by frequency (ν) and given in units of wavenumber (per centimeter).

Table V shows the mean values of the RDFs for each band, spectral region, and polarization estimated from the vicarious calibration data for VCC^{2009} to VCC^{2012}. Each band is divided into a short and a long spectral region in an attempt to determine a wavelength dependence of the RDFs, as was done in [14]. In 2009, bands 1 and 2 appear to have degraded more in the long-wavenumber spectral region, i.e., at shorter wavelengths. However, by VCC^{2010}, the wavelength dependence seems to have approached zero. Note that the decay in the S polarization is $\simeq$1%–2% greater in each band compared to the P polarization, presumably due to the oblique input angle and large polarization sensitivity of the beam splitter, as discussed in [2, Sec. 3.1.5].

The estimated radiometric degradations of TANSO-FTS as of July 2012 are $\simeq$18%–20% in B1 and 5%–7% in B2 and

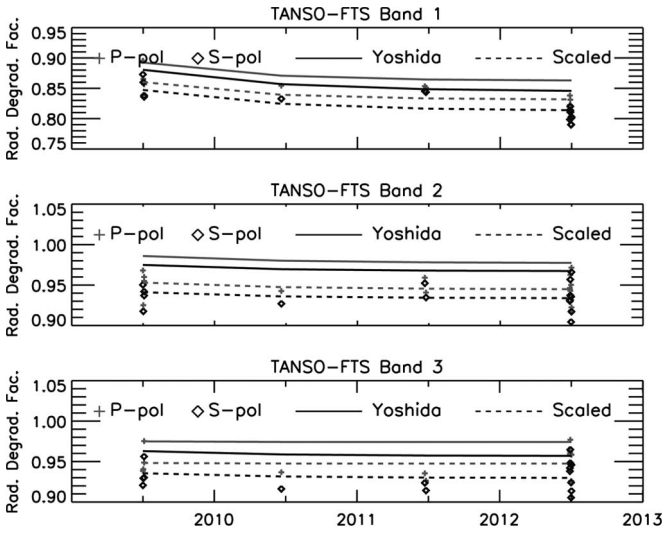

Fig. 4. Series plots of the TANSO-FTS RDFs relative to the prelaunch calibration. Rows correspond to spectral bands 1–3. The light gray plus symbols represent calibration points calculated from individual ASD measurements for the TANSO-FTS P polarization, while the dark gray diamonds represent the S polarization. The solid lines show the Yoshida model derived from the on-board solar diffuser data, tied to the mean of the original 2009 VCC RDFs reported in [8, Table IV] . The dashed lines represent a best fit scaled Yoshida value, as discussed in the text.

B3, relative to the prelaunch calibration. Based on the on-board solar diffuser data, a smooth monotonic degradation is expected. Therefore, the VCC^{2011} estimates seem to be too high (i.e., underestimates the degradation), particularly in B1 and B2. As will be discussed later, this could be an error in the estimated RDF due to the MODIS BRDF model used to correct the surface reflectances to the GOSAT geometry. The lower rows in Table V list the change in RDF relative to VCC^{2009}.

Fig. 4 shows the time series of the RDFs from the four annual VCCs (diamonds). The annual spreads in the RDFs for B1, polarization P, are as follows:

1) 2009: $N = 4$, 0.857–0.895 (0.039);
2) 2010: $N = 1$, 0.854–0.854 (0.000);
3) 2011: $N = 2$, 0.851–0.853 (0.002);
4) 2012: $N = 8$, 0.811–0.838 (0.027).

Note the smaller range of scatter in the reprocessed VCC^{2009} data, compared to the range 0.856–0.937 (0.081) reported in [8, Table IV]. Furthermore, the spread in the VCC^{2012} data is about three-quarters that of VCC^{2009}, even though there are twice the number of points. This is an indication of the improvement in the data collection, selection, and screening technique from VCC^{2009} to VCC^{2012}.

B. Tying the RDFs to a Relative Time-Dependent Model

Shown as solid lines in Fig. 4 are the RDF estimates provided by the analysis of the on-board solar diffuser data [14] (referred to as the Yoshida model), tied to the mean of the VCC^{2009} RDFs given in [8, Table IV]. An additional set of lines (dashed) shows new estimates of the RDFs, obtained by scaling the Yoshida values by a coefficient of a fit through all 15 VCC data points. The fit was determined by χ^2 minimization of the squared difference in RDFs over days $j = 1, \ldots, D$, from

TABLE VI
VALUES OF THE SCALING FACTOR ($\hat{C}$) USED TO BEST FIT THE YOSHIDA TIME-DEPENDENT DEGRADATION CURVE TO THE 15 VCC RDF POINTS

Spectral Region	B1 P	B1 S	B2 P	B2 S	B3 P	B3 S
Short ν	0.884	0.871	0.962	0.950	0.950	0.939
Long ν	0.879	0.864	0.955	0.942	0.951	0.938

TABLE VII
COMPARISON OF THE JUNE 2009 RDFS OBTAINED BY THREE DIFFERENT METHODS

Method	Description	B1 P	B1 S	B2 P	B2 S	B3 P	B3 S
1	Published VCC	0.893	0.881	0.986	0.975	0.975	0.963
2	Reprocessed VCC	0.874	0.857	0.948	0.933	0.948	0.931
3	VCC-Yoshida for day 157 DSL	0.861	0.848	0.952	0.940	0.946	0.934

Note; These values are given over the full spectral regions, as were those published in Table IV of [8].

the vicarious calibration (RDF^{VCC}) and a scaled Yoshida RDF ($\text{RDF}^{\text{Yoshida}} = C \cdot Y_j$)

$$\chi^2 = \sum_{j=1}^{D} \left[\text{RDF}_j^{\text{VCC}} - (C \cdot Y_j)\right]^2 \tag{3}$$

where Y_j is the time-dependent estimate from the Yoshida analysis on day j.

From (3), the scaling factor is determined from the least squares solution as

$$\hat{C}_{\lambda,\text{P|S}} = \frac{\sum_j \left[\text{RDF}_j^{\text{VCC}} \cdot Y_j\right]}{\sum_j Y_j^2}. \tag{4}$$

The symbols for spectral dependence and polarization in (3) and (4) have been omitted on the RHS. The values of $\hat{C}_{\lambda,\text{P|S}}$ deduced from the analysis of the 15 selected vicarious calibration data points are given in Table VI.

Using $\hat{C}_{\lambda,\text{P|S}}$, the RDFs at any time t (defined as days since launch, with $t = 0$ being January 23, 2009) can be obtained as follows:

$$\text{RDF}_{\lambda,\text{P|S}}(t) = \hat{C}_{\lambda,\text{P|S}} \cdot Y_{\lambda,\text{P|S}}(t) \tag{5}$$

where $Y(t)$ is the Yoshida time-dependent degradation taken from [14, eq. (7)]

$$Y(t) = d + e\ \exp[-f \cdot t] \tag{6}$$

with coefficients d, e, and f given in [14, Table III].

Corrected L1B spectra, denoted $\widetilde{\text{L1B}}_{\lambda,\text{P|S}}(t)$, are obtained as

$$\widetilde{\text{L1B}}_{\lambda,\text{P|S}}(t) = \frac{\text{L1B}_{\lambda,\text{P|S}}(t)}{\text{RDF}_{\lambda,\text{P|S}}(t)}. \tag{7}$$

Each time a new vicarious calibration is undertaken (the next one is scheduled for June 2013), the resultant $\text{RDF}_{\lambda,\text{P|S}}^{\text{VCC}}$ is used to update $\hat{C}_{\lambda,\text{P|S}}$. At that time, it is desirable to reprocess all L1B spectra via (5) and (7) to provide a consistent data set for use in the Level 2 (L2) retrieval algorithms.

TABLE VIII
NEW ESTIMATES OF RDFS AT SEVERAL KEY TIMES USING THE NEW COMBINED VCC–YOSHIDA ANALYSIS. THE VALUE DSL INDICATES THE DAYS SINCE LAUNCH. THE VALUES OF ΔRDF ARE CALCULATED RELATIVE TO THE VCC^{2009} VALUES

Date (yyyymmdd)	DSL	Spectral Region	B1 P	Δ RDF (%)	B1 S	Δ RDF (%)	B2 P	Δ RDF (%)	B2 S	Δ RDF (%)	B3 P	Δ RDF (%)	B3 S	Δ RDF (%)
2009-01-23	0	short ν	0.885	– 0.0%	0.871	– 0.0%	0.962	– 0.0%	0.950	– 0.0%	0.951	– 0.0%	0.940	– 0.0%
2009-01-23	0	long ν	0.880	– 0.0%	0.865	– 0.0%	0.955	– 0.0%	0.942	– 0.0%	0.953	– 0.0%	0.939	– 0.0%
2009-03-04	40	short ν	0.878	– 0.7%	0.865	– 0.7%	0.961	– 0.2%	0.949	– 0.2%	0.950	– 0.1%	0.939	– 0.1%
2009-03-04	40	long ν	0.873	– 0.7%	0.858	– 0.6%	0.953	– 0.2%	0.941	– 0.2%	0.951	– 0.2%	0.938	– 0.1%
2009-06-29	157	short ν	0.862	– 2.3%	0.850	– 2.2%	0.957	– 0.5%	0.945	– 0.5%	0.948	– 0.3%	0.936	– 0.4%
2009-06-29	157	long ν	0.858	– 2.2%	0.844	– 2.1%	0.949	– 0.5%	0.937	– 0.5%	0.948	– 0.5%	0.935	– 0.4%
2010-07-01	526	short ν	0.840	– 4.6%	0.826	– 4.6%	0.951	– 1.1%	0.940	– 1.1%	0.947	– 0.4%	0.932	– 0.8%
2010-07-01	526	long ν	0.838	– 4.3%	0.821	– 4.4%	0.943	– 1.1%	0.932	– 1.0%	0.948	– 0.5%	0.931	– 0.8%
2011-07-01	890	short ν	0.834	– 5.2%	0.818	– 5.4%	0.950	– 1.3%	0.938	– 1.2%	0.947	– 0.4%	0.931	– 0.9%
2011-07-01	890	long ν	0.832	– 4.8%	0.813	– 5.2%	0.941	– 1.3%	0.930	– 1.2%	0.948	– 0.5%	0.930	– 0.9%
2011-12-31	1072	short ν	0.832	– 5.3%	0.816	– 5.5%	0.949	– 1.3%	0.938	– 1.2%	0.947	– 0.4%	0.931	– 1.0%
2011-12-31	1072	long ν	0.831	– 4.9%	0.811	– 5.3%	0.941	– 1.4%	0.930	– 1.3%	0.948	– 0.5%	0.929	– 0.9%
2012-07-01	1256	short ν	0.832	– 5.3%	0.815	– 5.6%	0.949	– 1.3%	0.938	– 1.2%	0.947	– 0.4%	0.930	– 1.0%
2012-07-01	1256	long ν	0.831	– 5.0%	0.810	– 5.4%	0.941	– 1.4%	0.930	– 1.3%	0.948	– 0.5%	0.929	– 1.0%

Notes: Short ν_1 corresponds to frequency range 12900-13050 cm^{-1}.
Long ν_1 corresponds to frequency range 13050-13200 cm^{-1}.
Short ν_2 corresponds to frequency range 6150-6225 cm^{-1}.
Long ν_2 corresponds to frequency range 6225-6300 cm^{-1}.
Short ν_3 corresponds to frequency range 4800-4850 cm^{-1}.
Long ν_3 corresponds to frequency range 4850-4900 cm^{-1}.

C. Analysis of the Combined RDF Model

It is useful to explicitly compare the three sets of RDFs shown in Table VII to highlight the differences. The Method 1 values are simply the 2009 values published in [8, Table IV]. The Method 2 values are derived from the reprocessed VCC^{2009}. These values suggest ≃2%/4%/3% more degradation in B1/B2/B3 compared to Method 1 at the time of VCC^{2009}, i.e., the results presented in the original analysis given in [8] appear to have underestimated the radiometric degradation of TANSO-FTS. Finally, the Method 3 values are derived by combining the time-dependent Yoshida model with the reprocessed RDFs presented in this work. Method 3 suggests an additional 1%–1.5% degradation in B1 relative to Method 2. The changes in B2 and B3 were between −0.2% and 0.7% between Methods 2 and 3.

The $RDF_{\lambda,P|S}$ estimates using the newly described technique at several key times are presented in Table VIII. These values correspond to the dashed lines in Fig. 4. The results show a rapid degradation of about 0.7% in B1 within the first 40 days in orbit (at the time of the first on-board solar diffuser calibration), with more than 2% degradation by the time of the June 2009 (DSL 157) vicarious calibration. The degradations in B2 and B3 were less severe, about 0.5% by June 2009. The degradation in all bands doubled between the 2009 and 2010 VCCs. By December 31, 2011 (DSL 1072), B1 is shown to have degraded by ≃5% relative to the first day in orbit. At the same time, the degradations in B2 and B3 had increased to ≃1.5% and 0.5%–1.0%, respectively. This is in reasonable agreement with the results reported in [14] for the end of 2011. By the time of the June 2012 VCC (DSL 1256), the rate of change of the radiometric decay had tapered off to nearly zero in all bands. Based on these results, very little additional radiometric decay is anticipated for the remainder of the GOSAT lifetime.

To access the impact of the new estimates of the RDFs on retrieved X_{CO_2}, the ACOS L2 algorithm [6], [7] was run on both a land and an ocean data set using both the previous degradation correction model and the new estimates provided here. Although a full analysis is beyond the scope of the current work, we did observe an upward shift of ≃2 ppm in retrieved X_{CO_2}.

IV. DEGRADATION ESTIMATION OF TANSO-CAI

The radiometric vicarious calibration of TANSO-CAI short-wave spectral bands (0.38, 0.67, 0.87, and 1.60 μm) is simpler than that for TANSO-FTS since the surface reflectance was measured with the ASD over a 500-m-by-500-m area, the same size as a single TANSO-CAI pixel. Therefore, no spatial extrapolation of the surface reflectance is required to estimate the IFOV average albedo.

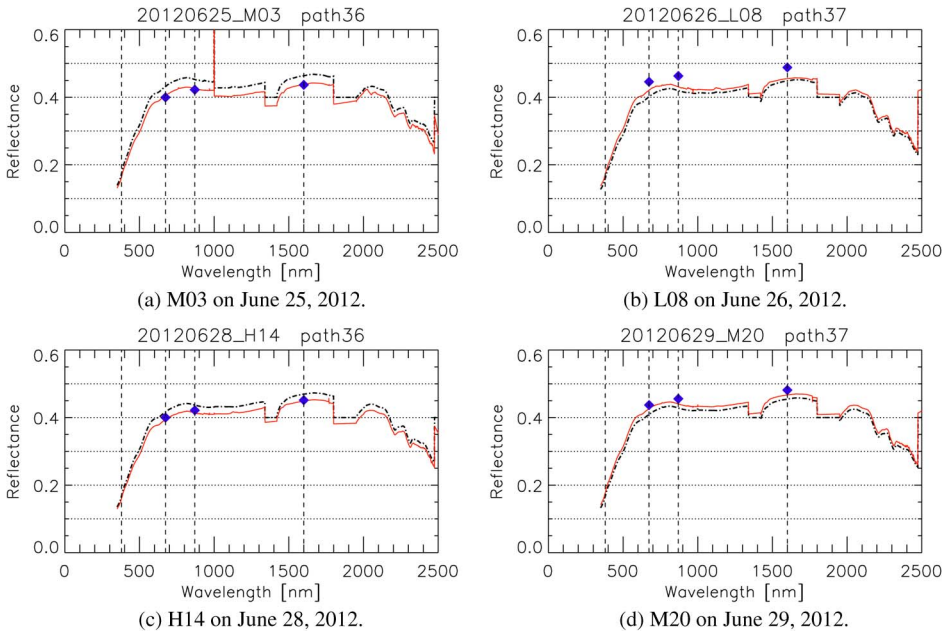

(a) M03 on June 25, 2012. (b) L08 on June 26, 2012.

(c) H14 on June 28, 2012. (d) M20 on June 29, 2012.

Fig. 5. Comparison of reflectance spectra with and without BRDF corrections at four sites during VCC^{2012}. The baseline reflectances calculated from the ASD measurements at nadir geometry are shown as black dash-dotted lines. The reflectances corrected by the off-nadir ASD measurements are shown as bold red lines. The reflectances corrected with the MODIS BRDF model are indicated by blue diamonds. (a) and (c) show the values using the ASD off-nadir angle of 20°, close to path 36 geometry, at sites M03 and H14, respectively. (b) and (d) show the values using the ASD off-nadir angle of 30°, close to path 37 geometry, at sites L08 and M20, respectively. The vertical dashed lines indicate the center wavelengths of the four TANSO-CAI spectral bands.

In the original VCC^{2009} data analysis described in [8], the surface BRDF effect for TANSO-CAI was not considered. Instead, an average of GOSAT overpass 36 days (westward viewing) and overpass 37 days (eastward viewing) was used. In this work, a BRDF correction has been applied to TANSO-CAI data using both the MODIS BRDF model and a set of off-nadir ASD measurements that were made during VCC^{2012}. These measurements were made at one site per day near the time of GOSAT overpass at off-nadir angles of 20° westward and 30° eastward viewing. This closely approximates the GOSAT viewing geometries for paths 36 and 37, respectively. The ratio of the off-nadir to nadir ASD reflectance spectra provides a proxy for the surface BRDF effect at that measurement geometry. Fig. 5 shows the uncorrected reflectance spectra compared with that corrected by the ASD BRDF proxy method as well as by the MODIS BRDF model at four sites. In some cases, the 16-day MODIS BRDF model is too sparse to accurately represent the non-Lambertian desert surface.

Table IX compares the RDFs calculated using both the MODIS BRDF correction and the correction using the VCC^{2012} off-nadir ASD measurements. The latter correction has less deviation and is more consistent between forward (path 36) and backward (path 37) optical scattering conditions.

Table X shows the annually estimated RDFs for TANSO-CAI derived by the comparison of the measured radiances to those modeled at the TOA using radiative transfer calculations. The methodology was the same as that presented in [8]. Three cases are shown:

1) no BRDF correction;
2) MODIS BRDF correction (MODIS does not have a band corresponding to TANSO-CAI 0.38 μm);
3) ASD off-nadir BRDF correction, where the VCC^{2012} measurements were applied to the previous years.

TABLE IX
ESTIMATED RDFS FOR TANSO-CAI FROM BRDF CORRECTION COMPARISON BETWEEN THE MODIS BRDF MODEL AND OFF-NADIR MEASURED DATA. THE MEAN AND STANDARD DEVIATION FROM THE FOUR SITES ARE GIVEN FOR EACH CHANNEL FOR BOTH THE MODIS AND OFF-NADIR TECHNIQUES

Date	Path	Site	BRDF correction	CAI-B1	CAI-B2	CAI-B3	CAI-B4
2012-6-28	36	M03	MODIS	N/A	0.964	0.99	0.868
			Off-nadir	0.783	0.954	0.983	0.868
		H14	MODIS	N/A	0.926	0.937	0.899
			Off-nadir	0.756	0.932	0.953	0.907
2012-6-29	37	M03	MODIS	N/A	0.927	0.918	NA
			Off-nadir	0.778	0.958	0.953	NA
		M20	MODIS	N/A	0.922	0.922	NA
			Off-nadir	0.768	0.945	0.954	NA
mean (μ)			MODIS	NA	0.935	0.942	0.884
stddev (σ)				NA	0.020	0.033	0.022
mean (μ)			Off-nadir	0.771	0.947	0.961	0.888
stddev (σ)				0.012	0.012	0.015	0.028

In the lower portion of the table, the percent differences relative to the VCC^{2009} values are shown. Also included are the values derived from the analysis of a set of space-based measurements of several Sahara desert sites, as discussed in [2]. Based on these data, there appears to be a problem in 2011, as the predicted degradation is significantly larger for B2 and B3. For VCC^{2011}, there was a rain event prior to the campaign. Hence, the MODIS BRDF model may not be accurate. The data over the Sahara desert also indicate that the rate of degradation becomes slower for TANSO-CAI.

Fig. 6 shows the time series plots of the TANSO-CAI RDFs for each of the four bands. The three shaded symbols represent the results when no BRDF correction is applied, compared to application of the MODIS BRDF correction, as well as the off-nadir ASD BRDF correction. As the signal-to-noise ratio of

TABLE X
(TOP) ESTIMATED RDFS FOR TANSO-CAI FROM THE RRV VCCS RELATIVE TO THE PRELAUNCH CALIBRATION AND (BOTTOM) RELATIVE PERCENT CHANGE FROM VCC^{2009}

CAI Band	BRDF Correction	2009	2010	2011	2012
B1	None	0.846	0.799	0.816	0.772
	MODIS	N/A	N/A	N/A	N/A
	ASD®	0.862	0.836	0.797	0.772
B2	None	1.019	0.939	1.013	0.931
	MODIS	1.032	0.989	0.892	0.921
	ASD®	1.035	1.026	0.982	0.937
B3	None	0.979	0.937	1.002	0.947
	MODIS	0.988	0.982	0.882	0.936
	ASD®	0.991	1.027	0.979	0.955
B4	None	NA	0.828	N/A	0.822
	MODIS	0.899	0.862	N/A	0.867
	ASD®	0.860	0.896	N/A	0.870

CAI Band	BRDF Correction	Δ 2009	Δ 2010	Δ 2011	Δ 2012
B1	None	N/A	-5.6%	-3.6%	-8.8%
	MODIS	N/A	N/A	N/A	N/A
	ASD®	N/A	-3.1%	-7.6%	-10.5%
	Sahara	N/A	-1.7%	-1.7%	-5.0%
B2	None	N/A	-7.9%	-0.6%	-8.7%
	MODIS	N/A	-4.1%	-13.6%	-10.8%
	ASD®	N/A	-0.9%	-5.1%	-9.5%
	Sahara	N/A	-3.9%	-4.8%	-6.0%
B3	None	N/A	-4.3%	+2.3%	-3.2%
	MODIS	N/A	-0.6%	-10.7%	-5.3%
	ASD®	N/A	+3.6%	-1.2%	-3.6%
	Sahara	N/A	-0.7%	-0.7%	-1.6%
B4	None	N/A	N/A	N/A	N/A
	MODIS	N/A	-4.1%	N/A	-3.6%
	ASD®	N/A	+4.1%	N/A	+1.2%
	Sahara	N/A	-0.3%	-0.9%	-2.7%

TANSO-CAI is lower and only a few points per campaign are available to fit, the deviation is larger for TANSO-FTS. Note that there are no TANSO-CAI data for spectral band 4 in 2011. This is due to the retention of data sets from only GOSAT overpass 37 days based on the ASD stability analysis. On overpass 37 days, the viewing angle of TANSO-CAI is oblique such that the footprint of band 4 is too large to fall within RRV.

V. ERROR BUDGET ESTIMATE

This section discusses our best estimate of the uncertainties in the vicarious calibration of TANSO-FTS solar bands using the results from VCC^{2012}. The original study, presented in [8, Sec. VII-A], discussed the uncertainties in terms of radiance

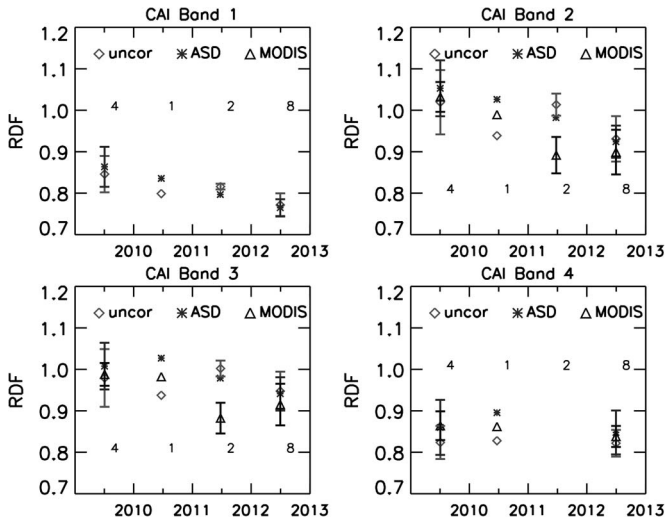

Fig. 6. Time series plots of the TANSO-CAI RDFs for four spectral bands. The points represent the mean value for each year of individual ASD measurements, with one standard deviation error indicated by vertical bars. The shaded symbols represent results for (light gray diamonds) no BRDF correction, (medium gray asterisks) application of an off-nadir ASD correction, and (dark gray triangles) application of a MODIS BRDF correction.

error with no account for spectral bands. In this study, we present the errors separately for each spectral band in terms of the estimated change in the RDF due to the change in some variable. We assume equal errors in both P and S polarizations. We note that some sources of error are random and will therefore integrate down when multiple calibration points are averaged during any single calibration campaign. Other error sources are systematic and will therefore not integrate down. The present discussion does not distinguish between the two. We simply provide a worse case uncertainty in the calculated RDF and remind the reader that these errors exist.

The accuracy of each of the major sources of uncertainty and the corresponding error in the calculated RDFs for each solar band are summarized in Table XI. An itemized discussion of each source of uncertainty follows.

There is neither evidence for a change in the TANSO-FTS prelaunch calibration that is applied to the measured radiances nor a change to the solar irradiance data that are used in the radiative transfer calculations. Therefore, the uncertainties for these two items remain the same as those reported in [8, Table VI], i.e., 3% and 2%, respectively, for all spectral bands.

The pointing accuracy of TANSO-FTS has been much improved since VCC^{2009} by changing from five- to three-point cross-track scan mode and by making geometric corrections using the on-board camera. The high accuracy of the target pointing mode used when viewing RRV has been verified by the on-board camera, yielding little error in recent calibrations. The estimated pointing uncertainty is highly repeatable, and pointing precision has been reduced from 1 to 0.5 km. Based on the discussion of MODIS radiance pixel selection presented in Section II-C, an RDF error of 0.005 was assigned for all spectral bands.

The basic assumptions in the radiative transfer code and the effects of neglected polarization have not changed since

TABLE XI
APPROXIMATE ERROR BUDGET FOR THE VICARIOUS CALIBRATION OF TANSO-FTS. ERRORS ARE GIVEN IN TERMS OF THE CHANGE IN RDF FOR EACH SPECTRAL BAND

Class	Process/ measurement	Accuracy	RDF Error B1	B2	B3
Radiance conversion	TANSO prelaunch calibration	±3%	0.03	0.03	0.03
Solar irradiance	Toon model	±2%	0.02	0.02	0.02
TANSO-FTS IFOV	Mechanical pointing	0.5 km	0.005	0.005	0.005
Radiative transfer model	Assumptions and polarization		0.005	0.005	0.005
Meteorology	Uncertainty in Scattering type (aerosol or cloud)		0.02	0.02	0.03
	Total AOT	±100%	0.02	0.02	0.03
	Vertical temperature profile	±0.5 K	$\ll$0.01	$\ll$0.01	$\ll$0.01
	Vertical pressure profile	±1 hPa	$\ll$0.01	$\ll$0.01	$\ll$0.01
	Vertical humidity profile	±5%	$\ll$0.01	$\ll$0.01	$\ll$0.01
BRDF correction	MODIS model		0.01	0.01	0.01
Surface reflectance measurements	Spectralon® reflectance	±0.5%	0.005	0.005	0.005
	Spectralon® BRDF correction	±1%	0.01	0.01	0.01
	ASD® response stability	±0.5%	0.005	0.005	0.005
	MODIS radiance product		0.01	0.01	0.01
	surface BRDF changes over measurement period		0.02	0.02	0.035
	Thin cloud contamination	1%	0.01	0.01	0.01
TANSO-FTS RMS error			0.055	0.055	0.070

VCC^{2009}; hence, an estimated radiance error of 0.5% is still used, which translates directly to an RDF error of 0.005. The vertical profiles of meteorological fields (pressure, temperature, and humidity) used in the radiative transfer model are presumed to be quite accurate since they were measured daily by local radiosonde launches. The estimated radiance and RDF errors therefore remain as they were in the VCC^{2009} study, i.e., $\ll 1\%$.

As described in [8, Sec. IV-D], the column integrated AOT value used in the radiative transfer calculation is taken from that measured by the AERONET station located at the RRV playa [10]. A simple model of the scattering material is selected based on the calculated Ångström exponent (α): continental aerosol when $\alpha > 0.75$ and cirrus cloud when $\alpha < 0.75$. In [8], the value of α was calculated using the 500 and 1020 nm wavelength pair. However, during VCC^{2012}, there were mathematical instabilities when the AOT at 1020 nm approached zero. We therefore selected the 500 and 870 nm wavelength pair to provide a more robust calculation of α.

To determine the uncertainty in our aerosol model, we calculated radiances using vertical distributions of both continental aerosol, located 2–4 km above the surface, and a cirrus layer at 8–10 km. The AOT was held fixed ($\simeq$0.03–0.05 at 500 nm for the 4 days during VCC^{2012}), and the change in the RDFs with respect to a Rayleigh-only scattering atmosphere was calculated.

The RDFs were shifted $\simeq$0.015 in all three bands when using the continental aerosol layer, while shifts of $\simeq$0.0, 0.02, and 0.03 in B1, B2, and B3, respectively, were observed for the cirrus layer, relative to the Rayleigh-only scenario. We assigned these shifts as errors to reflect uncertainties in the type and vertical distribution of the scattering layer. An additional test indicated that doubling the AOT (to $\simeq$0.06–0.10) yielded a doubling in the RDF error. We therefore assigned additional errors of 0.02, 0.02, and 0.03 for B1, B2, and B3, respectively, to account for uncertainties in the total column AOT.

To test the sensitivity of the vicarious calibration to the selection of the BRDF correction, RDFs were calculated for VCC^{2012} using MODIS MCD43B1 granules for days 153, 161, and 169, all covering rain-free periods according to the Duckwater, NV, USA, rain gauge. The percent change in RDF was less than 0.001 in all three bands, regardless of the chosen MODIS BRDF file. An additional run was made using MODIS BRDF granule for day 185, which contained a $\simeq$13.5-mm rain event over a 4-day duration in the middle of the 16-day collection period. The RDFs were found to be higher (less degradation) by $\simeq$0.011, 0.015, and 0.021 in B1, B2, and B3, respectively, due to the use of this MODIS BRDF file. We have assigned a nominal error of 0.01 in all spectral bands to account for uncertainties in the MODIS BRDF model.

There are a number of uncertainties in the calculation of the surface reflectance derived from the ASD measurements. Testing indicated that a 1% shift in the calculated surface reflectance values yields slightly less than 0.01 change in RDFs. For simplicity, we have adopted a one-to-one correspondence in reflectance and RDF.

The first two uncertainties associated with surface reflectance are related to the Spectralon panel, which requires both a reflectance and a BRDF correction. Spectralon panel comparisons performed during and after VCCs indicate that the panels have little degradation in the wavelength regions of interest. Agreement of the panels to within 0.5% was found for wavelengths greater than 0.760 μm, where the reflectance is much less sensitive to contamination and panel-to-panel variation. The Spectralon BRDF correction is estimated to have a 1% accuracy, which produces a corresponding 1% uncertainty in the calculated reflectance.

Additional errors in the surface reflectance calculations are due to the ASD instrument and the measurement technique. Repeatability of the ASD has been estimated at $\simeq$0.3% based on field testing. An upper error of 0.005 was adopted for the budget.

As was previously discussed, great care was taken to select the most representative MODIS radiance product possible. Even so, there is some uncertainty related to this choice in how well it represents the real surface. A detailed analysis indicates that the resultant RDFs can change by up to 0.015 based on the selection of the MODIS radiance. However, 0.005 was a more typical change. We therefore selected 0.01 as a reasonable estimate of this error.

Even after accounting for the change in SZA over the duration of the ASD measurements, some small time dependence often existed in the calculated reflectance time series. It is thought that this is due to very slight changes in the atmosphere and/or unaccounted for changes in the BRDF of the desert surface. Based on statistical threshold test number 3 described in Section II-B, upper error bounds of 0.02, 0.02, and 0.035 were assigned to B1, B2, and B3, respectively.

The use of pyranometers during the field campaign suggested that, occasionally, a very thin cloud, not visible to the naked eye, partially contaminated the scene over the duration of the ASD measurement sequence. An analysis of these data suggests an accuracy of about 1%, resulting in a reflectance error of 1%, yielding an RDF error of approximately 0.01.

When all sources of error are assumed to be independent, the rms value can be calculated to provide an upper bound estimate of the total error in the vicarious calibration results. We again remind the reader that many of these error sources are random and will therefore integrate down when averaging many vicarious calibration points. For TANSO-FTS, the upper bound rms errors are estimated to be 0.055, 0.055, and 0.070 in B1–B3, respectively. These results are similar to the 7% radiance error budget assigned to all bands in [8, Table VI].

VI. Discussion and Conclusion

In this paper, we have presented analysis from 4 years of vicarious calibrations of the short-wave bands of the GOSAT instruments using data from the RRV calibration site. Many techniques were introduced to reduce the error in estimates of the radiometric degradation of both TANSO-FTS and TANSO-CAI. A careful analysis of the MODIS radiance and BRDF products was performed in order to select the best set of inputs used in the radiative transfer calculations needed to compute radiances for the RDF estimate.

For TANSO-FTS, the new estimates of RDFs were used to constrain the relative time-dependent model that was recently introduced by Yoshida *et al.* [14]. A key result of the Yoshida analysis was the implementation of spectrally dependent RDFs to correct a time-dependent χ^2 and spectral residual in the National Institute for Environmental Studies SWIR L2 retrieval algorithm. Unfortunately, it is difficult to interpret a meaningful spectral dependence from our analysis as the data from individual days are somewhat erratic. However, by combining the time-dependent Yoshida model derived from on-board solar diffuser data with the 2009–2012 vicarious calibration results, we think that the best estimates of the RDFs are made. We suggest implementation of the method presented in this paper to all future GOSAT SWIR L1B spectra prior to performing L2 inversions.

A detailed uncertainty analysis was performed for TANSO-FTS, in which the change in RDFs as a result of major sources of uncertainty was analyzed for each spectral band. The rms errors in the reported RDFs are estimated to be 0.055, 0.055, and 0.070 in B1, B2, and B3, respectively.

For TANSO-CAI, a BRDF correction was implemented using both the MODIS model and off-nadir ASD *in situ* measurements performed during VCC^{2012}. The results indicate that the ASD BRDF proxy is more stable than the MODIS model. A time-dependent degradation model for TANSO-CAI can be made by combining VCC and Sahara data as was done for TANSO-FTS using the VCC and solar diffuser calibration data. However, there is no AOT or radiosonde data available over the Sahara, and the RDF calculation from the VCCs also has a large deviation. Therefore, further work is required prior to implementation of a time-dependent degradation model for TANSO-CAI.

Acknowledgment

The authors would like to thank two anonymous reviewers for providing helpful comments. The authors would also like to thank the following individuals for helping with the planning and measurements: N. Goto from the Japan Aerospace Exploration Agency; H. Tan and J. Laderos from the National Aeronautics and Space Administration (NASA)'s Jet Propulsion Laboratory (JPL); E. Yates, L. Iraci, M. Lowenstein, and E. Sheffner from NASA's Ames Research Team; and the H211 Alpha Team, consisting of pilots K. Ambrose, D. Simmons, and R. Simone and ground staff B. Quiambao, R. Fisher, and J. Lee. The authors would also like to thank V. Gandarillas from Purdue University; R. Rosenberg from the California Institute of Technology; R. O. Knuteson, J. Roman, and E. Garms from the University of Wisconsin; and K. Schiro from the University of California Los Angeles. The authors would also like to thank T. Matsunaga, A. Kamei, and the Level 2 Data Teams of the National Institute for Environmental Studies and Atmospheric Carbon Observations from Space (ACOS). Part of the research described here was carried out at JPL, California Institute of Technology, under a contract with NASA. The Colorado State University contributions to the ACOS task were supported by NASA Contract 1439002.

References

[1] A. Kuze, H. Suto, M. Nakajima, and T. Hamazaki, "Thermal And Near infrared Sensor for carbon Observation Fourier-Transform Spectrometer on the Greenhouse Gases Observing Satellite for greenhouse gases monitoring," *Appl. Opt.*, vol. 48, no. 35, pp. 6716–6733, Dec. 2009.

[2] A. Kuze, H. Suto, K. Shiomi, T. Urabe, M. Nakajima, J. Yoshida, T. Kawashima, Y. Yamamoto, F. Kataoka, and H. Buijs, "Level 1 algorithms for TANSO on GOSAT: Processing and on-orbit calibrations," *Atmos. Meas. Tech.*, vol. 5, no. 10, pp. 2447–2467, Oct. 2012.

[3] H. Ishida, T. Y. Nakajima, T. Yokota, N. Kikuchi, and H. Watanabe, "Investigation of GOSAT TANSO-CAI cloud screening ability through an intersatellite comparison," *J. Appl. Meteorol. Clim.*, vol. 50, no. 7, pp. 1571–1586, 2011.

[4] F. Kataoka, R. O. Knuteson, A. Kuze, H. Suto, K. Shiomi, M. Harada, E. M. Garms, J. A. Roman, D. C. Tobin, J. K. Taylor, H. E. Revercomb, N. Sekio, R. Higuchi, and Y. Mitomi, "TIR spectral radiance calibration of the GOSAT satellite borne TANSO-FTS with the aircraft-based S-HIS and the ground-based S-AERI at the Railroad Valley desert playa," *IEEE Trans. Geosci. Remote Sens.*, vol. 52, no. 1, Jan. 2014, to be published. [Online]. Available: http://ieeexplore.ieee.org

[5] Y. Yoshida, Y. Ota, N. Eguchi, N. Kikuchi, K. Nobuta, H. Tran, I. Morino, and T. Yokota, "Retrieval algorithm for CO_2 and CH_4 column abundances from short-wavelength infrared spectral observations by the Greenhouse Gases Observing Satellite," *Atmos. Meas. Tech.*, vol. 4, no. 4, pp. 717–734, Apr. 2011.

[6] C. W. O'Dell, B. Connor, H. Bösch, D. O'Brien, C. Frankenberg, R. Castano, M. Christi, D. Crisp, A. Eldering, B. Fisher, M. Gunson, J. McDuffie, C. E. Miller, V. Natraj, F. Oyafuso, I. Polonsky, M. Smyth, T. Taylor, G. C. Toon, P. O. Wennberg, and D. Wunch, "The ACOS CO_2 retrieval algorithm—Part 1: Description and validation against

synthetic observations," *Atmos. Meas. Tech.*, vol. 5, no. 1, pp. 99–121, Jan. 2012.

[7] D. Crisp, B. M. Fisher, C. O'Dell, C. Frankenberg, R. Basilio, H. Bösch, L. R. Brown, R. Castano, B. Connor, N. M. Deutscher, A. Eldering, D. Griffith, M. Gunson, A. Kuze, L. Mandrake, J. McDuffie, J. Messerschmidt, C. E. Miller, I. Morino, V. Natraj, J. Notholt, D. M. O'Brien, F. Oyafuso, I. Polonsky, J. Robinson, R. Salawitch, V. Sherlock, M. Smyth, H. Suto, T. E. Taylor, D. R. Thompson, P. O. Wennberg, D. Wunch, and Y. L. Yung, "The ACOS CO_2 retrieval algorithm—Part II: Global X_{CO_2} data characterization," *Atmos. Meas. Tech.*, vol. 5, no. 4, pp. 687–707, Apr. 2012.

[8] A. Kuze, D. M. O'Brien, T. E. Taylor, J. O. Day, C. W. O'Dell, F. Kataoka, M. Yoshida, Y. Mitomi, C. Bruegge, H. Pollock, R. Basilio, M. Helmlinger, T. Matsunaga, S. Kawakami, K. Shiomi, T. Urabe, and H. Suto, "Vicarious calibration of the GOSAT sensors using the Railroad Valley desert playa," *IEEE Trans. Geosci. Remote Sens.*, vol. 49, no. 5, pp. 1781–1795, May 2011.

[9] F. Sakuma, C. Bruegge, D. Rider, D. Brown, S. Geier, S. Kawakami, and A. Kuze, "OCO/GOSAT preflight cross-calibration experiment," *IEEE Trans. Geosci. Remote Sens.*, vol. 48, no. 1, pp. 585–599, Jan. 2010.

[10] B. Holben, T. Eck, I. Slutsker, D. Tanre, J. Buis, A. Setzer, E. Vermote, J. Reagan, Y. Kaufman, T. Nakajima, F. Lavenu, I. Jankowiak, and A. Smirnov, "AERONET—A federated instrument network and data archive for aerosol characterization," *Remote Sens. Environ.*, vol. 66, no. 1, pp. 1–16, Oct. 1998.

[11] W. Wanner, X. Li, and A. H. Strahler, "On the derivation of kernels for kernel-driven models of bidirectional reflectance," *J. Geophys. Res.*, vol. 100, no. D10, pp. 21 077–21 089, Oct. 1995.

[12] W. Lucht, C. B. Schaaf, and A. H. Strahler, "An algorithm for the retrieval of albedo from space using semiempirical BRDF models," *IEEE Trans. Geosci. Remote Sens.*, vol. 38, no. 2, pp. 977–998, Mar. 2000.

[13] C. J. Bruegge, M. C. Helmlinger, J. E. Conel, B. J. Gaitley, and W. A. Abdou, "PARABOLA III: A sphere-scanning radiometer for field determination of surface anisotropic reflectance functions," *Remote Sens. Rev.*, vol. 19, no. 1-4, pp. 75–94, 2000.

[14] Y. Yoshida, N. Kikuchi, and T. Yokota, "On-orbit radiometric calibration of SWIR bands of TANSO-FTS onboard GOSAT," *Atmos. Meas. Tech.*, vol. 5, no. 10, pp. 2515–2523, Oct. 2012.

Authors' photographs and biographies not available at the time of publication.